

Fast and Accurate Spatiotemporal Fusion Based Upon Extreme Learning Machine

Xun Liu, *Student Member, IEEE*, Chenwei Deng, *Senior Member, IEEE*, Shuigen Wang, *Student Member, IEEE*, Guang-Bin Huang, *Senior Member, IEEE*, Baojun Zhao, and Paula Lauren, *Student Member, IEEE*

Abstract—Spatiotemporal fusion is important in providing high spatial resolution earth observations with a dense time series, and recently, learning-based fusion methods have been attracting broad interest. These algorithms project image patches onto a feature space with the enforcement of a simple mapping to predict the fine resolution patches from the corresponding coarse ones. However, the sophisticated projection, e.g., sparse representation, is always computationally complex and difficult to be implemented on large patches, which cannot grasp enough local structural information in the coarse patches. To address these issues, a novel spatiotemporal fusion method is proposed in this letter, using a powerful learning technique, i.e., extreme learning machine (ELM). Unlike traditional approaches, we devote to learning a mapping function on difference images directly, rather than the sophisticated feature representation followed by a simple mapping. Characterized by good generalization performance and fast speed, the ELM is employed to achieve accurate and fast fine patches prediction. The proposed algorithm is evaluated by five actual data sets of Landsat enhanced thematic mapper plus-moderate resolution imaging spectroradiometer acquisitions and experimental results show that our method obtains better fusion results while achieving much greater speed.

Index Terms—Extreme learning machine (ELM), feature representation, local structural information, mapping function, spatiotemporal image fusion.

I. INTRODUCTION

DUE to the hardware limitations and budget constraints, there is a tradeoff between temporal coverage and spatial resolution in current satellite remote sensing systems. Generally, it is difficult for a single satellite to provide high-spatial-resolution earth observations with a dense time series. The images acquired from Landsat satellites are with fine spatial resolutions in a range of 6–30 m, however, the long revisit cycles (16–26 days) of these satellites limit their potential use in the detection of rapid surface changes [1]. On the other hand, moderate resolution imaging spectroradiometer (MODIS) carried on Terra/Aqua satellites could

provide (daily) observations, but with coarse spatial resolutions ranging from 250 to 1000 m, which is deemed insufficient for monitoring land cover changes in heterogeneous landscapes [2]. For this purpose, spatiotemporal fusion has been identified as a promising way to provide satellite images with both high spatial and temporal resolutions.

In the past decade, a number of spatiotemporal fusion algorithms have been proposed. The most successful method has been the spatial and temporal adaptive reflectance fusion model (STARFM) [3]. With STARFM, daily high spatial resolution reflectance images are reconstructed empirically through similar neighboring pixels weighted by spectral, temporal, and spatial differences. Several other algorithms have also been developed for improving the fusion results [4]–[6], which have a critical constraint. The constraint of these models requires that little change of the land cover type happens between the known and predicted dates. This results in good performance only for predicting pixels with phenology changes. Furthermore, trying to model complex and nonlinear relationships between central and neighboring pixels poses other challenges when using simple weighting in the spatial domain [7].

Recently, learning-based spatiotemporal fusion approaches have drawn particular attention by considering phenology and type reflectance changes during an observation period in a unified framework [8]–[10]. By exploiting the structure similarity of the same scenes, these algorithms attempt to find correlations between fine and coarse images in the sparse domain. The fusion procedure can be divided into two steps: feature representation and feature mapping. The first step entails sparse coding performed to project the coarse image patches onto a feature space. The second step ensures that the sparse coefficients are mapped into a fine dictionary through a simple predefined function (equal to [8] and [9], or linear correlation [10]), for reconstructing the fine patches. Learning-based methods mainly focus on feature representation, which involves optimizing the coefficients and dictionaries of fine and coarse image patches. However, the feature mapping function between fine and coarse patches are quite straightforward.

In addition, due to the computational complexity of sparse coding, the size of image patches for fusion is generally small; on the other hand, it is also known that the magnification factors between fine and coarse images are practically large. In this case, limited local structural information can be exploited for prediction of the fine image patches. For example, in [10]–[12], the size of patches is set as 7×7 , while the magnification factors between Landsat (30 m) and

Manuscript received May 18, 2016; revised September 19, 2016; accepted October 17, 2016. This work was supported by the National Natural Science Foundation of China under Grant 61301090. (Corresponding author: Chenwei Deng.)

X. Liu, C. Deng, S. Wang, and B. Zhao are with the School of Information and Electronics, Beijing Institute of Technology, Beijing 100081, China (e-mail: cxdeng@bit.edu.cn).

G.-B. Huang is with the School of Electrical and Electronic Engineering, Nanyang Technological University, Singapore 639798.

P. Lauren is with the School of Engineering and Computer Science, Oakland University, Rochester, MI 48309 USA.

Color versions of one or more of the figures in this letter are available online at <http://ieeexplore.ieee.org>.

Digital Object Identifier 10.1109/LGRS.2016.2622726

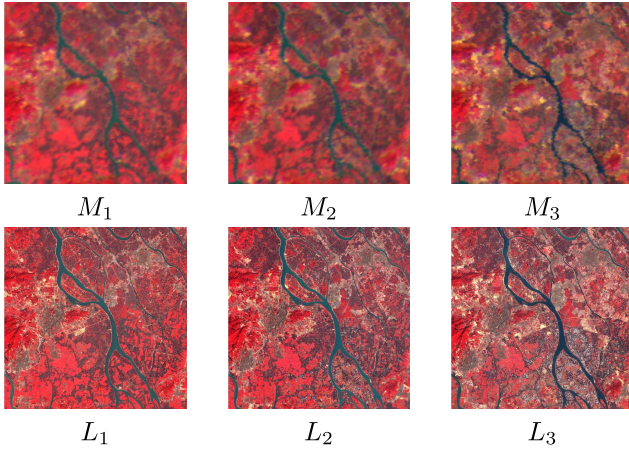


Fig. 1. Composites surface reflectance of MODIS (top row) and Landsat (bottom row) data acquired from data set 4 in Table I.

MODIS (250–500 m) images are from 8 to 16. This means that each patch in prediction is actually less than one interpolated pixel in coarse images, and little structural information utilized in coarse patches naturally results in a deterioration of the prediction performance.

Instead of sophisticated feature representation followed by a simple feature mapping in the existing methods, we focus on learning an efficient mapping function just on simple features in this letter. The utilization of raw pixels of difference images are considered as image features, and the extreme learning machine (ELM) is explored to train the mapping function. Characterized by good generalization performance and fast speed of ELM [12], fast and accurate fine patch prediction can be achieved. Moreover, due to the simplicity of the proposed method, a larger patch size can be adopted to make use of richer structural information in coarse patches for prediction, and thus the fusion performance can be further boosted.

It is worth noting that Bai *et al.* [13] also used ELM for deriving land surface temperature images with both high spatial and temporal resolutions. However, ELM is adopted for preprocessing (to enhance Landsat images) [13], and not for the subsequent spatiotemporal fusion. While in our work, ELM is employed to predict the Landsat images using the corresponding MODIS ones, and by doing so, the spatiotemporal fusion is achieved.

II. METHODOLOGY

In this letter, our aim is to predict a fine resolution image at t_2 using the coarse images at t_2 , and two pairs of fine and coarse images at t_1 and t_3 . Specifically, as shown in Fig. 1, two pairs of Landsat (L_1, L_3) and MODIS (M_1, M_3) reflectance images at t_1 and t_3 , and MODIS image (M_2) at t_2 are available to predict the Landsat image (L_2) at t_2 .

The flowchart of the proposed algorithm is shown in Fig. 2. It should be mentioned that, following the work in [5], our method is performed on difference images rather than the original ones. Let L_{ij} and M_{ij} represent the differences in the Landsat and MODIS images between t_i and t_j , respectively. Note that without sophisticated projection to a feature space, the raw pixels of L_{13} and M_{13} are used for feature mapping, and the ELM is employed to train the mapping function.

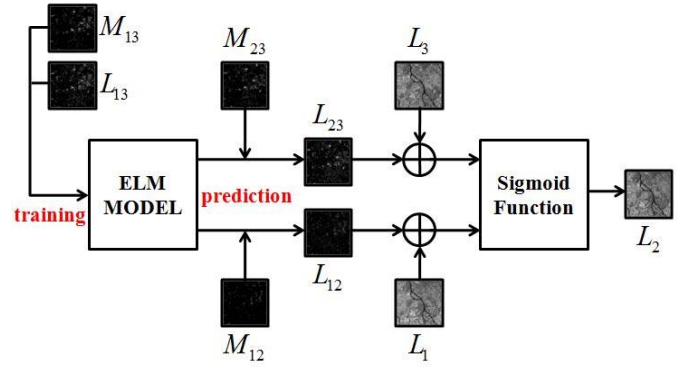


Fig. 2. Schematic of the proposed spatiotemporal fusion method. Here, L_i and M_i denote the Landsat and MODIS images at t_i date, while L_{ij} and M_{ij} denote the differences in Landsat and MODIS images between t_i and t_j , respectively.

Then, given the corresponding M_{12} and M_{23} , L_{12} and L_{23} could be obtained from the trained function. A sigmoid function is applied to reconstruct the final Landsat image (L_2) using L_1 and L_3 , with their predicted difference images L_{12} and L_{23} .

A. ELM Training for Feature Mapping

In this letter, the original patches of difference images are directly utilized as features for the ELM training of mapping function. Let $P_{L_{13}} = [p_{L_{13}}^1, p_{L_{13}}^2, \dots, p_{L_{13}}^N] \in R^{n^2 \times N}$ and $P_{M_{13}} = [p_{M_{13}}^1, p_{M_{13}}^2, \dots, p_{M_{13}}^N] \in R^{n^2 \times N}$ be the randomly selected patches from L_{13} and M_{13} , and all the patches have been rearranged into column vectors. Here, N denotes the patch numbers for training, and n^2 denotes vector dimension of the patches.

ELM is an effective solution for single hidden layer feed-forward neural networks, whose hidden layer parameters need not be adjusted [14]. Specifically, the hidden layer parameters are randomly assigned and subsequently the output weights are analytically calculated. It has been demonstrated that ELM not only has excellent generalization performance but also achieves fast speed in numerous applications, such as object detection [15], image quality assessment [16], and hyperspectral image classification [17]. Inspired by these previous achievements, ELM is adopted for spatiotemporal fusion in this letter.

The goal of ELM training is to find a mapping $f(p_{M_{13}}^i)$, which has the smallest deviation from the corresponding Landsat patch $f(p_{L_{13}}^i)$ for all the training samples. Technically, the ELM regression model with K hidden neurons and an activation function $g(\cdot)$ can be expressed as

$$p_{L_{13}}^i = \sum_{j=1}^K \beta_j g(w_j \cdot p_{M_{13}}^i + b_j), \quad i = 1, \dots, N \quad (1)$$

where β_j denotes the output weights connecting the j th hidden neurons and the output nodes; w_j and b_j represent the input weights and the bias of the j th hidden neuron, and are generated randomly.

Considering N training samples from the selected patches above, (1) can be compactly written as

$$H\beta = P_{L_{13}} \quad (2)$$

where H is the $N \times K$ output matrix of the hidden layer in ELM, and can be represented as

$$H = \begin{pmatrix} g(w_1 \cdot p_{M_{13}}^1 + b_1) & \dots & g(w_K \cdot p_{M_{13}}^1 + b_K) \\ \vdots & \ddots & \vdots \\ g(w_1 \cdot p_{M_{13}}^N + b_1) & \dots & g(w_K \cdot p_{M_{13}}^N + b_K) \end{pmatrix}. \quad (3)$$

So far, training the ELM regression model is simply equivalent to finding a least-squares solution of the above equation, and the minimal norm least square method is employed. Thus, the parameter β could be analytically estimated [11], [18] as

$$\beta = H^\dagger P_{L_{13}} \quad (4)$$

where H^\dagger is the Moore–Penrose generalized inverse of the hidden layer output matrix H .

B. ELM-Based Fine Image Prediction

Once the ELM mapping function is trained, we could predict the fine difference image L_{12} using the coarse image M_{12} . First, we apply the sliding window technique to divide M_{12} into overlapping $n \times n$ patches $\{p_{M_{12}}^T\}$ from the upper left to the lower right with a step length of s pixels, where T is the total number of patches. Subsequently, let $p_{M_{12}}^i$ denote the i th image patch of M_{12} , and the corresponding fine patch $p_{L_{12}}^i$ in L_{12} can be obtained by the trained ELM model

$$p_{L_{12}}^i = \sum_{j=1}^K \beta_j g(w_j \cdot p_{M_{12}}^i + b_j), \quad i = 1, \dots, T. \quad (5)$$

Finally, each fine patch is reshaped and put into its original position in L_{12} . As the patches are overlapped, each pixel's value in L_{12} is averaged over its accumulation times. In the same way, the fine difference image L_{13} could be predicted by M_{13} .

It is worth noting that there is a high efficiency in the prediction process made possible from using the ELM, as it does not necessitate adjusting the hidden node parameters of ELM networks. Therefore, our fusion method is especially advantageous to be implemented on high-dimensional data compared with traditional approaches.

C. Reconstruction

Having the predicted difference images, we attempt to reconstruct the fine image through an adaptive local weighting approach as follows:

$$L_2 = W_1 * (L_1 + L_{12}) + W_3 * (L_3 - L_{23}) \quad (6)$$

where W_1 and W_3 are the weighting parameters for the predicted image L_2 from L_1 and L_3 , respectively.

We prefer to choose the predicted result from more similar reference images, and the degree of changes between two MODIS images is employed to measure the reliability of the predicted Landsat images. That is to say, when the absolute value of M_{i2} , i.e., the difference between the images in t_i and t_2 , is smaller, the prediction would be more reliable, thus it is reasonable for us to give larger weights to the predicted images from date t_i . Therefore, a sigmoid

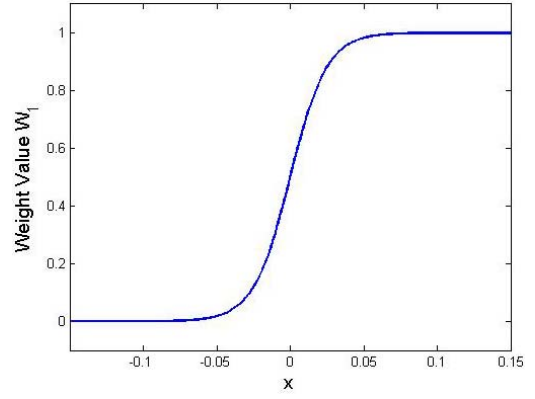


Fig. 3. Sigmoid function for calculating weighting parameters.

TABLE I

DETAILED INFORMATION OF FIVE TESTED DATA SETS

| Data Set | Location | t_1 | t_2 | t_3 |
|----------|-------------------|------------|------------|------------|
| 1 | 54°36'N, 104°51'W | 2001.05.24 | 2001.07.11 | 2001.08.12 |
| 2 | 37°06'N, 77°06'W | 2002.01.25 | 2002.02.26 | 2002.05.17 |
| 3 | 28°33'N, 116°37'E | 2004.05.05 | 2004.07.24 | 2004.08.09 |
| 4 | 22°37'N, 113°06'E | 2000.11.01 | 2002.11.07 | 2004.11.28 |
| 5 | 22°36'N, 113°58'E | 2000.11.01 | 2002.11.07 | 2004.11.28 |

function is employed to calculate the weighting parameters with an illustration in Fig. 3. The weight maps can be modeled as

$$W_1 = \frac{1}{1 + e^{-k \cdot x}} \quad (7)$$

where k controls the curve shape of the sigmoid function and is empirically set as 80 in our experiments. x is calculated by

$$x = |M_{23}| - |M_{12}|. \quad (8)$$

Also, we can have

$$W_3 = 1 - W_1. \quad (9)$$

III. EXPERIMENTAL RESULTS AND ANALYSIS

In this section, extensive experiments were performed on five data sets of Landsat ETM+ (30 m) and MODIS (250–500 m) reflectance images to verify the proposed method. These tested data sets cover complex study areas with a size of 30 km \times 30 km, and the locations of these images with acquisition dates are shown in Table I. Herein, the Landsat ETM+ images were obtained from the United States Geological Survey (<http://earthexplorer.usgs.gov/>), which have been corrected using the 6S approach [1]. The MODIS images were available in the Land Processes Distributed Active Archive Center (<http://lpdaac.usgs.gov/lpdaac/>), and then reprojected and resampled with the MODIS Reprojection Tool.

The proposed ELM-based spatiotemporal fusion model (ELM-FM) was compared with two well-known fusion algorithms: STARFM [3] and SPSTFM [8]. Three widely used metrics were applied for evaluating the fusion performance of the difference methods: absolute average difference (AAD), root-mean-square error (RMSE), and structural similarity (SSIM) [19].

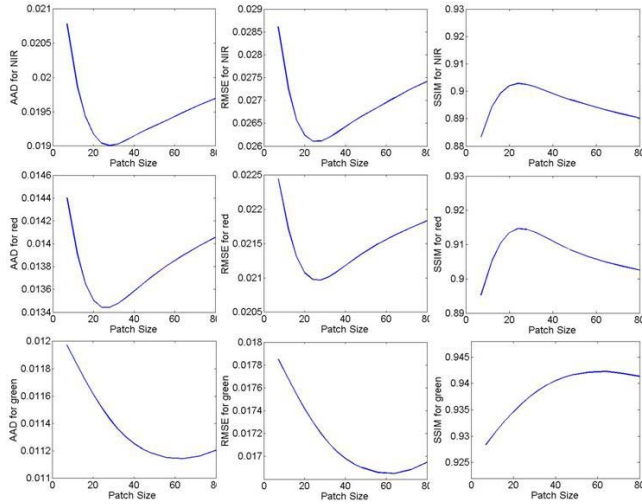


Fig. 4. Fusion performance of the proposed ELM-FM with different patch sizes n . In the simulation, five tested data sets are used and the average results are demonstrated.

A. Parameter Analysis

For STARFM and SPSTFM, the default parameters given by the respective authors were adopted in experiments. For the proposed algorithm, two main parameters, i.e., the patch size $n \times n$ and the step size s , need to be adjusted.

The influence of parameter n is depicted in Fig. 4. As the value of n increases, AAD and RMSE become smaller and SSIM gets larger, which means that the fusion performance improves. However, if n is too large this will result in bad fusion performance for all the evaluation metrics. This is due to the fact that a small patch may not contain enough structural information, while a large patch would lead to unstable prediction. Therefore, n should have an appropriate value. From Fig. 4, we can see that when $n = 28$, the near infrared response (NIR) and red bands achieve the best performance, while the green band has the best results in the case of $n = 64$. The reason is that the green band (500 m) of MODIS images is much coarser than the red or NIR bands (250 m), and thus, n needs to be larger to grasp enough structural information for prediction.

The fusion performance of ELM-FM with different step sizes was also compared. As different patch sizes were used for prediction, different step sizes should be used accordingly. Let s be the step size of the red and NIR bands, and for simplicity, the step size of the green band was set as $2.3s$ ($\approx 68/24$). The average values of indices for the three bands are shown in Table II. As demonstrated in the table, when the value of s increases, the fusion performance is deteriorated due to the blockiness effect. Meanwhile, the proposed ELM-FM achieves much greater speed. In order to balance the fusion performance and the computing burden, the step size s was set as 10 in the simulation.

B. Experimental Results

The average objective performance of the five tested data sets for different fusion methods is presented in Table III. For the three indices (AAD, RMSE, and SSIM), SPSTFM has better results than that of STARFM, due to the effective

TABLE II
FUSION PERFORMANCE OF ELM-FM WITH DIFFERENT
STEP SIZE s IN PREDICTION PROCESS

| s | 1 | 2 | 5 | 10 | 20 | 28 |
|---------|--------|--------|--------|--------|--------|--------|
| AAD | 0.0144 | 0.0145 | 0.0145 | 0.0146 | 0.0147 | 0.0149 |
| RMSE | 0.0210 | 0.0211 | 0.0213 | 0.0215 | 0.0217 | 0.0221 |
| SSIM | 0.9171 | 0.9169 | 0.9163 | 0.9152 | 0.9127 | 0.9089 |
| TIME(s) | 1039 | 284 | 91.05 | 18.14 | 14.99 | 13.22 |

TABLE III
QUANTITATIVE ASSESSMENT OF DIFFERENT METHODS

| Index | band | STARFM | SPSTFM | Proposed |
|-------|-------|--------|--------|---------------|
| AAD | NIR | 0.0217 | 0.0207 | 0.0191 |
| | red | 0.0149 | 0.0144 | 0.0135 |
| | green | 0.0124 | 0.0120 | 0.0113 |
| RMSE | NIR | 0.0308 | 0.0289 | 0.0263 |
| | red | 0.0242 | 0.0225 | 0.0212 |
| | green | 0.0191 | 0.0181 | 0.0169 |
| SSIM | NIR | 0.8546 | 0.8763 | 0.9016 |
| | red | 0.8867 | 0.8923 | 0.9129 |
| | green | 0.9212 | 0.9271 | 0.9412 |

representation in coupled dictionaries; while the proposed method significantly outperforms STARFM and SPSTFM for all the three bands in the experiments. These results indicate that the proposed ELM-FM can not only reconstruct the most accurate Landsat surface reflectance images (the smallest AAD and RMSE), but also present more structural details in actual Landsat images (the largest SSIM).

Apart from the objective evaluation, a set of representative results from data set 4 are subjectively demonstrated in Fig. 5. Furthermore, a close-up view is presented in the bottom-right of each subpicture to have a better observation. As shown in Fig. 5, the proposed method produces sharper edges than other algorithms without any obvious artifacts in the image. On the contrary, some details are invisible in the fused image obtained by STARFM, such as the cross roads; while serious artifacts (see the black region on the right side) are introduced into the fused image of SPSTFM.

From both the objective and subjective verifications, it can be seen that, compared with STARFM and SPSTFM, the fused image obtained by the proposed ELM fusion model is the closest result to the actual Landsat image.

C. Computational Efficiency Analysis

The computing time of different spatiotemporal fusion methods were compared in Table IV and the experiments were performed on a computer equipped with 2.40-GHz Intel-i7 CPU and 16-GB DDR3 RAM. All the codes accessed from different platforms were wrapped by MATLAB software for a fair comparison.

As shown in Table IV, the STARFM takes an average of 94.97 s for the fusion of the tested data sets, of size $1000 \times 1000 \times 3$. This is due to the fact that simple linear operation is required in the STARFM. Whereas the SPSTFM method takes more than 30 min as it requires solving

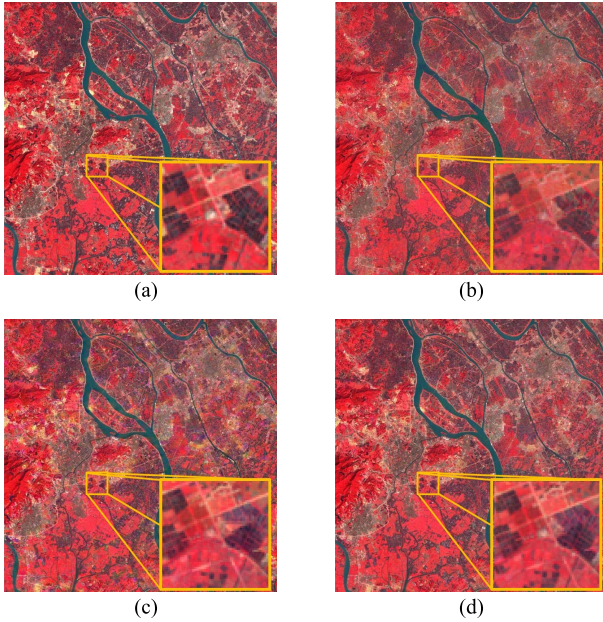


Fig. 5. Spatiotemporal fusion results obtained by different methods. (a) Actual Landsat image. (b) Predicted by STARFM. (c) Predicted by SPSTFM. (d) Predicted by proposed ELM-FM.

TABLE IV

COMPUTATION EFFICIENCY OF DIFFERENT METHODS

| Index | STARFM | SPSTFM | ELM-FM |
|---------|--------|--------|--------------|
| TIME(s) | 94.97 | 1835 | 18.14 |

sophisticated optimization problems in training and prediction. As for ELM-FM, from Section II, one can note that the hidden nodes, input weights w_j , and hidden layer biases b_j of ELM are all randomly generated, and the output weighting vector β is analytically calculated. Furthermore, the prediction process is also fully feedforward and no complicated optimization problem needs to be solved. Therefore, the proposed ELM-FM achieves extremely fast fusion speed compared with the existing fusion methods.

IV. CONCLUSION

In this letter, we have presented a fast and accurate spatiotemporal image fusion method. Instead of sophisticated feature representation followed by a simple feature mapping in the existing models, we have paid particular attention to building a feature mapping function between the raw pixels of coarse and fine images, through an efficient learning technique, named ELM. By doing so, the proposed approach achieves accurate fine patch prediction and is remarkably fast, which leads to a larger patch size in prediction to make use of richer structural information. Extensive experiments have been conducted using actual Landsat and MODIS images. Compared with the STARFM and SPSTFM methods, our work achieves

the best performance at much greater speed, which is quite helpful in large-scale satellite image spatiotemporal fusion.

REFERENCES

- [1] J. G. Masek *et al.*, "A Landsat surface reflectance dataset for North America, 1990–2000," *IEEE Geosci. Remote Sens. Lett.*, vol. 3, no. 1, pp. 68–72, Jan. 2006.
- [2] M. A. Friedl *et al.*, "Global land cover mapping from modis: Algorithms and early results," *Remote Sens. Environ.*, vol. 83, nos. 1–2, pp. 287–302, Nov. 2002.
- [3] F. Gao, J. Masek, M. Schwaller, and F. Hall, "On the blending of the Landsat and MODIS surface reflectance: Predicting daily Landsat surface reflectance," *IEEE Trans. Geosci. Remote Sens.*, vol. 44, no. 8, pp. 2207–2218, Aug. 2006.
- [4] X. Zhu, J. Chen, F. Gao, X. Chen, and J. G. Masek, "An enhanced spatial and temporal adaptive reflectance fusion model for complex heterogeneous regions," *Remote Sens. Environ.*, vol. 114, no. 11, pp. 2610–2623, Nov. 2010.
- [5] T. Hilker *et al.*, "Generation of dense time series synthetic Landsat data through data blending with modis using a spatial and temporal adaptive reflectance fusion model," *Remote Sens. Environ.*, vol. 113, no. 9, pp. 1988–1999, Sep. 2009.
- [6] Q. Weng, P. Fu, and F. Gao, "Generating daily land surface temperature at Landsat resolution by fusing Landsat and modis data," *Remote Sens. Environ.*, vol. 145, pp. 55–67, Apr. 2014.
- [7] B. Chen, B. Huang, and B. Xu, "Comparison of spatiotemporal fusion models: A review," *Remote Sens.*, vol. 7, no. 2, pp. 1798–1835, Feb. 2015.
- [8] B. Huang and H. Song, "Spatiotemporal reflectance fusion via sparse representation," *IEEE Trans. Geosci. Remote Sens.*, vol. 50, no. 10, pp. 3707–3716, Oct. 2012.
- [9] H. Song and B. Huang, "Spatiotemporal satellite image fusion through one-pair image learning," *IEEE Trans. Geosci. Remote Sens.*, vol. 51, no. 4, pp. 1883–1896, Apr. 2013.
- [10] B. Wu, B. Huang, and L. Zhang, "An error-bound-regularized sparse coding for spatiotemporal reflectance fusion," *IEEE Trans. Geosci. Remote Sens.*, vol. 53, no. 12, pp. 6791–6803, Dec. 2015.
- [11] G.-B. Huang, Q.-Y. Zhu, and C.-K. Siew, "Extreme learning machine: Theory and applications," *Neurocomputing*, vol. 70, nos. 1–3, pp. 489–501, 2006.
- [12] G.-B. Huang, H. Zhou, X. Ding, and R. Zhang, "Extreme learning machine for regression and multiclass classification," *IEEE Trans. Syst., Man, Cybern. B, Cybern.*, vol. 42, no. 2, pp. 513–529, Apr. 2012.
- [13] Y. Bai, M. S. Wong, W.-Z. Shi, L.-X. Wu, and K. Qin, "Advancing of land surface temperature retrieval using extreme learning machine and spatio-temporal adaptive data fusion algorithm," *Remote Sens.*, vol. 7, no. 4, pp. 4424–4441, 2015.
- [14] J. Tang, C. Deng, and G.-B. Huang, "Extreme learning machine for multilayer perceptron," *IEEE Trans. Neural Netw. Learn. Syst.*, vol. 27, no. 4, pp. 809–821, Apr. 2016.
- [15] J. Tang, C. Deng, G.-B. Huang, and B. Zhao, "Compressed-domain ship detection on spaceborne optical image using deep neural network and extreme learning machine," *IEEE Trans. Geosci. Remote Sens.*, vol. 53, no. 3, pp. 1174–1185, Mar. 2015.
- [16] S. Wang, C. Deng, W. Lin, G.-B. Huang, and B. Zhao, "NMF-based image quality assessment using extreme learning machine," *IEEE Trans. Cybern.*, to be published. doi: 10.1109/TCYB.2015.2512852.
- [17] Y. Bazi, N. Alajlan, F. Melgani, H. AlHichri, S. Malek, and R. R. Yager, "Differential evolution extreme learning machine for the classification of hyperspectral images," *IEEE Geosci. Remote Sens. Lett.*, vol. 11, no. 6, pp. 1066–1070, Jun. 2014.
- [18] A. Ben-Israel and T. N. Greville, *Generalized Inverses: Theory and Applications*. New York, NY, USA: Springer-Verlag, 2003.
- [19] Z. Wang, A. C. Bovik, H. R. Sheikh, and E. P. Simoncelli, "Image quality assessment: From error visibility to structural similarity," *IEEE Trans. Image Process.*, vol. 13, no. 4, pp. 600–612, Apr. 2004.